Modeling and experimental study of the effect of pore water velocity on the spectral induced polarization signature in porous Media

K. Tsukanov[1], I. Assa[1], and N. Schwartz[1]

[1]The Institute of Environmental Sciences, The Robert H. Smith Faculty of Agriculture, Food and Environment, The Hebrew University of Jerusalem, Rehovot 76100 Israel.

Corresponding author: Nimrod Schwartz (nimrod.schwartz@mail.huji.ac.il)

Key Points:

- Polarization and time constant decrease with pore water velocity.
- The decrease in polarization is attributed to the deformation of the electrical double layer.
- Accounting for ion advection flux in the EDL results in a decrease in the time constant.

Abstract

Induced polarization (IP) is increasingly applied for hydrological, environmental and agricultural purposes. Interpretation of IP data is based on understanding the relationship between the IP signature and the porous media property of interest. Mechanistic models on the IP phenomenon rely on the Poisson-Nernst-Plank equations, where diffusion and electromigration fluxes are the driving forces of charge transport and are directly related to IP. However, to our knowledge, the impact of advection flux on IP was not investigated experimentally and was not considered in any IP model. In this work, we measured the spectral IP (SIP) signature of porous media under varying flow conditions, in addition to developing and solving a model for SIP signature of porous media, which takes flow into consideration. The experimental and the model results demonstrate that as bulk velocity increases, polarization and relaxation time decrease. Using a numerical model, we established that fluid flow near the particle deforms the electrical double layer (EDL) structure, accounting for the observed reduction in polarization. We found a qualitative agreement between the model and the measurements. Still, the model overestimates the impact of flow rate on SIP signature, which we explain in terms of the flow boundary conditions. Overall, our results demonstrate the sensitivity of the SIP signature to fluid flow, highlighting the need to consider fluid velocity in the interpretation of the SIP signature of porous media, and opening an exciting new direction for noninvasive measurements of fluid flow at the EDL scale.

1 Introduction

The induced polarization (IP) method is a geophysical technique increasingly applied to characterize, monitor, and map the shallow subsurface. For example, IP was successfully used to monitor biogeochemical processes, such as growth and decay of bacteria (Mellage et al., 2018), FeS biomineralization (Slater et al., 2007), calcite precipitation (Zhang et al., 2012), degradation of petroleum hydrocarbon contaminants (Kimak et al., 2019), and more (for a recent review, see Kessouri et al. (2019)). The IP method also exhibits a potential for monitoring freezing and thawing processes in soil and other porous material (Coperey et al., 2019), the aggregate size distribution of clay suspensions (Leroy et al., 2017; Schwartz et al., 2020), and plant roots (Weigand & Kemna, 2019; Tsukanov & Schwartz, 2020). The success of the IP method in detecting and monitoring a large variety of processes is attributed to its sensitivity to the bulk (water content, formation factor, and salinity) and interfacial (e.g., surface charge density, ionic mobility, conductivity, etc.) properties of the porous media.

IP measurements are performed by applying an electrical field through two electrodes, and measuring the resulting potential with two other electrodes. In the spectral IP (SIP), a sinusoidal current (I) is applied at a broad frequency range (typically 0.01 Hz to 10 kHz), the resulting potential (U) is measured, and the complex electrical impedance ($Z = U/I$) is calculated. Considering the geometry of the sample, the impedance can be converted to complex conductivity (σ^*), which typically decomposes to in-phase conductivity (σ') and quadrature conductivity (σ''), according to: $\sigma^* = \sigma' + i\sigma''$, where i is the imaginary unit. In porous media, the in-phase conductivity is mostly related to the pore water electrical conductivity, water saturation, electrical conductivity of the solid surface, and to geometrical features of the porous media, such as porosity and tortuosity (Vinegar & Waxman, 1984; Weller et al., 2011; Revil, 2013).

The quadrature conductivity is related to the polarization of the porous media and is generally frequency-dependent (Kemna et al., 2012). At the low-frequency range (up to 1 kHz), σ'' is related to polarization of the electrical double layer (EDL). The EDL consists of a surface charge that is compensated by an oppositely charged ionic atmosphere (Adamson & Gast, 1997). The application of an electrical field external to the EDL leads to ion migration and polarization (Dukhin & Shilov, 1974). In porous media, where the solid particles are in contact, polarization occurs at the Stern layer, which is the innermost part (closest to the surface) of the EDL (Leroy et al., 2008), and at narrow passages in the pore space (pore throat), in what is known as membrane polarization (Titov et al., 2002). According to the Stern-layer polarization model, polarization is caused by the tangential movement of the mobile counter-ions (Revil & Florsch, 2010). Polarization of the Stern layer is related to the physicochemical properties of the solid−liquid interface, such as the surface-site density of the chemical species, their mobility, and their valence. Polarization is also related to the particle size distribution of the porous media (Jougnot et al., 2010; Vaudelet et al., 2011; Weller et al., 2011).

Membrane polarization describes polarization as the accumulation of ions at the pore throat, where the diffuse layers of two or more particles merge, creating a zone with a different ion transference number (defined as the fraction of current carried by a specific ion) (Titov et al., 2004; Volkmann & Klitzsch, 2010). As in the Stern-layer model, polarization in the membrane model is also related to the physicochemical properties of the solid−fluid interface (e.g., Bücker & Hördt, 2013). The main difference between the Stern- and the membrane-polarization models is the length scale of polarization. In the Stern-layer model, the governing length scale is the particle radius, whereas in the membrane polarization model, it is the pore

size (Revil et al., 2012). Shefer et al., (2013) noted that polarization is induced by both Stern and membrane-polarization mechanisms. A recent model by Bücker et al. (2019) coupled the two mechanisms, and investigated their relative contribution to the SIP signature of porous media.

Mechanistic modeling of the low-frequency polarization of porous media, for both Stern-layer and membrane polarization, involves the solution of the Poisson-Nernst-Planck (PNP) equations, where the divergence of the diffusive flux ($\boldsymbol{J_D}$), and the electromigration flux ($\boldsymbol{J_e}$) control the temporal change in the ion concentration field. Considering a simple binary electrolyte, the PNP equations are given by (Newman & Thomas-Alyea, 2004):

$$\frac{\partial c_{\pm}}{\partial t} = -\nabla \cdot (\boldsymbol{J_D} + \boldsymbol{J_e}) = \nabla \cdot \left(D\nabla c_{\pm} + \frac{zeD}{k_B T} c_{\pm} \nabla \psi \right), \quad (1)$$

$$\nabla(\varepsilon \nabla \psi) = -\rho, \quad (2)$$

where $c_{\pm}$ is the concentration, D is the diffusion coefficient, z is the valency, e is the elementary charge, k_B is the Boltzmann coefficient, T is the temperature, ψ is the electric potential, ε is the electric permittivity of the electrolyte, and ρ is the volume charge density. With the appropriate set of boundary conditions, Eq. (1) and (2) can be solved for the concentration and potential fields. The gradients of the concentration and potential are obtained from the solution, and with the assistance of Ohm's law, the complex conductivity is obtained (Titov et al., 2002; Leroy et al., 2008; Revil, 2013; Bücker et al., 2019). The approach described above significantly improves the understanding of the processes controlling the SIP response of porous media and allows linking the electrical signature to important subsurface properties and processes.

Another essential transport mechanism for ions (charge carriers) in porous media is the advection flux ($\boldsymbol{J_a} = \boldsymbol{v} c_{\pm}$, where $\boldsymbol{v}$ is the fluid velocity). Indeed, in the electrochemical literature, transport processes are described by the sum of the diffusive, electromigration, and advection fluxes ($\boldsymbol{J_T} = \boldsymbol{J_D} + \boldsymbol{J_e} + \boldsymbol{J_a}$, where $\boldsymbol{J_T}$ is the total flux) (e.g., Lyklema, 1995; Newman & Thomas-Alyea, 2004; Bazant et al., 2009; DeLacey & White, 1981; Shilov et al., 2001 and references therein). Important electrokinetic phenomena in porous media are related to the advection flux. For example, applying an external electric field to porous media exerts electrostatic forces on the ions. As a result, drag forces on the fluid drive the electroosmotic flow of water (Zhang & Wang, 2017). Similarly, pressure-driven flow in porous media generates an electrical current in the EDL (known as streaming potential, e.g., Soldi et al.,

2018). Despite its central role in the transport of ions in porous media, to our knowledge, the effect of the advection flux on the SIP response of porous media hasn't been established experimentally or considered in mechanistic models for SIP of porous media. Therefore, this research aims to develop a mechanistic understanding of the advection flux's role in the SIP response of porous media.

2 Material and Methods

2.1 Measuring the SIP response of soil at different water fluxes

To measure the impact of water flux on soil's SIP response, we used three identical polyvinyl chloride columns with an inner diameter of 3 cm and a length of 30 cm. The columns were equipped with four electrode ports, allowing the insertion of potential and current electrodes. We used 6 mm diameter brass electrodes for both the current and potential electrodes. The current electrodes were 8 cm long and crossed the entire sample. The potential electrodes were 5 cm long and were retracted in their respective holes to prevent electrode polarization. Electrical contact between the potential electrodes and the sample was ensured along the electrolyte. To convert impedance to conductivity, we measured the impedance (Z) of a series of electrolytes with different electrical conductivities, σ_w, and computed the conversion factor (G) using $G = \sigma_w/\mathrm{Re}(Z)$. To obtain the polarization produced by the sample holder (which should be minimal), we measured the electrical spectrum of the electrolyte used for the experiment ($\sigma_w = 2500$ μS cm^{-1}), and found that up to 1 kHz, the phase shift (φ) was lower than 0.5 mrad. The SIP signals were recorded using the PSIP impedance spectrometer (Ontash & Ermac Inc., NJ, USA) at 52 logarithmically spaced intervals, from 0.01 to 1000 Hz.

We used two types of porous materials: an oven-dried, sieved (2 mm screen) red sandy loam soil (thereinafter, Hamra soil) with 92% sand, 2% silt, and 6% clay, and quartz sand (Agat Minerals, Yeruham, Israel) with 97% sand and 3% silt (measured using PARIO, Meter group, Germany). Before packing, the soil and sand were mixed with an electrolyte to a gravimetric water content of 0.083. Packing was performed by adding small portions of soil or sand ($\sim$ 50 g) to the column and gently compressing it. This packing procedure was found to provide excellent repeatability (the average bulk density were 1.6 ± 0.001 g cm^{-3}, and 1.47 ± 0.0006 g cm^{-3} for the Hamra soil and the quartz sand, respectively). After packing and to obtain chemical equilibrium between the electrolyte and the mineral surface, we washed the soil with a concentrated $CaCl_2$ (0.1M) solution until the water volume was exchanged three times (three pore volumes) and then with 0.005M $CaCl_2$ solution until the electrical conductivities of the

inlet and outlet solutions equalized (EC = 1200 μS cm^{-1}). Full water saturation during the experiments was ensured by placing the columns vertically and directing the flow from the column bottom to its top.

We measured the SIP response of the soil at six different water fluxes (from 0 to 0.08 mm s^{-1}). We chose these fluxes as they are in the range of the porous materials` saturated hydraulic conductivity (0.027 mm s^{-1} for the Hamra soil and 0.075 mm s^{-1} for the quartz sand. Measured by KSAT, Meter group, Germany). We controlled the fluxes with a peristaltic pump (Masterflex L/S series, Cole-Parmer Inc., IL, USA). We started the SIP measurements at a zero flux and recorded SIP signals ~ 20 min after each increase in the water flux. To test possible hysteresis effects, following the SIP measurement at the highest water flux, we reduced the flow rate and repeated the SIP measurements for the same water fluxes, but this time for receding fluxes. Note that during the experiments, water was continuously flowing in the system.

We analyzed the electrical spectra using the Cole-Cole model (Tarasov & Titov, 2013).

$$\sigma^* = \sigma_0 \left(1 + \frac{m}{1-m}\left(1 - \frac{1}{1+(i\omega\tau)^c}\right)\right), \tag{3}$$

where σ_0 is the DC electrical conductivity, m is the chargeability, which is related to the polarization magnitude, τ is the Cole-Cole time constant, $\omega = 2\pi f$, is the angular frequency, and c is the Cole-Cole exponent. Fitting was performed using SciPy non-linear least-squares package (Virtanen et al., 2020). Note that we limit our analysis to the first relaxation process and fit the electrical spectra between 0.01 Hz and 5 Hz.

2.2 Modeling the effect of ion advection flux on the SIP response of porous media

To account for the effect of ion advection flux on the SIP response of porous media, we added the ion advection flux to the total ion flux, such that: $\boldsymbol{J_T} = \boldsymbol{J_D} + \boldsymbol{J_e} + \boldsymbol{J_a}$. Substituting the total flux with the continuity equation ($\partial c_{\pm}/\partial \mathrm{t} = -\nabla \cdot \mathbf{J_T}$) leads to a modified Nernst-Planck equation:

$$\frac{\partial c_{\pm}}{\partial t} = \nabla(\boldsymbol{J_D} + \boldsymbol{J_e} + \boldsymbol{J_a}) = \nabla\left(D\nabla c_{\pm} + \frac{zeD}{k_B T} c_{\pm}\nabla\psi - \boldsymbol{v}c_{\pm}\right). \tag{4}$$

Eq. 4 is similar to Eq. 1, except for the last term on the RHS (right hand side) of Eq. 4 that represents the ion advection flux. Assuming an incompressible fluid and a small Reynolds

number (typical for flow in porous media), the fluid velocity can be described by the Stokes equations:

$$\eta \nabla^2 \boldsymbol{v} - \nabla p = 0, \tag{5}$$

$$\nabla \cdot \boldsymbol{v} = 0, \tag{6}$$

where η is the dynamic viscosity, and p is the fluid pressure. Eq. (2), (4), (5), and (6) are known as the Poisson-Nernst-Planck-Stokes (PNP-S) equations, and are the governing equations in our model.

Our modeling approach is based on the recent work of (Bücker et al., 2019). The model domain is a single spherical grain embedded in a binary electrolyte (see Fig. 1). The domain is excited by a weak oscillating electric field, $\boldsymbol{E} = \boldsymbol{E_0}\exp(i\omega t)$, where $\boldsymbol{E_0}$ is the magnitude of the electric field. The solution strategy is based on the perturbation theory, with the assumption that the applied field ($\boldsymbol{E}$) results in a small deviation from equilibrium. Under this assumption, the concentration is expressed as the sum of the equilibrium concentration (c_j^0) and the perturbed concentration ($\widetilde{c_j}$), such that: $c_j = c_j^0 + \widetilde{c_j}\exp(i\omega t)$. Similarly, the electric potential is: $\psi = \psi^0 + \tilde{\psi}\exp(i\omega t)$, where ψ^0 and $\tilde{\psi}$ are the equilibrium and perturbed electrical potential, respectively.

To obtain c_j^0 and ψ^0, we solved the steady-state PNP-S equations:

$$\nabla\left(D\nabla c_{\pm}^0 \pm \frac{eD}{k_B T} c_{\pm}^0 \nabla\psi^0 - \boldsymbol{v} c_{\pm}^0\right) = 0, \tag{7}$$

$$\nabla(\varepsilon\nabla\psi^0) = (\mathrm{ez}_{-}c_{-}^0 + ez_{+}c_{+}^0). \tag{8}$$

The following boundary conditions were maintained: far from the particle, the concentration is $c_+^0 = c_-^0 = 1\ \mathrm{mol\ m^{-3}} \times\ \mathrm{N_A}$, where $\mathrm{N_A}$ is the Avogadro number, and the electric potential is zero. At the particle surface, the normal ionic flux is set to zero ($\boldsymbol{n} \cdot \boldsymbol{J_T^0}|_{\mathrm{r_{surf}}} = 0$). Using Gauss's law, the electric field on the particle surface is given by:

$$-\boldsymbol{n}\nabla\psi^0|_{\mathrm{r_{surf}}} = \frac{\Sigma_d^0}{\varepsilon}, \tag{9}$$

where Σ_d^0 is the net surface-charge density (this is the surface charge density of the mineral minus the surface charge density at the Stern layer), and is assumed to be constant in time, and

distributed uniformly over the particle, $\boldsymbol{n}$ is the unit normal vector pointed outward the grain's surface (Fig. 1).

To obtain the velocity field ($\boldsymbol{v}$), we assumed that the electroosmotic flow is negligible (i.e., we did not couple between fluid velocity and the electric field), and solved Stokes equations (Eq. 5 and Eq. 6) on the domain shown in Fig. 1. The flow was induced by a pressure gradient between the upper and lower boundaries, such that $p(x = 2.5L) = 0$, and $p(x = 2.5L) = p_0$, where p_0 is the applied pressure. Typically, on a solid surface, the velocity $\boldsymbol{v_s}$ is given by a no-slip boundary condition (i.e., $\boldsymbol{v_s} = 0$). However, a large body of evidence demonstrates that the small-scale interactions at the solid-liquid interface lead to various slip behavior (e.g., Joseph et al., 2006; Willmott, 2008; Zhu & Granick, 2002), and that factor such as degree of wetting, pressure gradient, surface charge, and surface roughness impact the slip velocity (Lauga et al., 2007). Furthermore, in electrokinetic systems, such as the one considered here, the transport of ions in the EDL drags fluid, producing slip velocity (Bazant, 2011). Accordingly, and following Ristenpart et al. (2007), we set the velocity normal to the solid surface as zero ($\boldsymbol{v_s} \cdot \boldsymbol{n} = 0$, i.e., slip boundary condition). For comparison, we also tested the case of no-slip boundary conditions.

Under the assumption that the perturbed variables follow harmonic dependency on time (due to the time-harmonic external electric field $\boldsymbol{E}$), the perturbed parts of Eq. 4 and Eq. 2 are written as:

$$i\omega\widetilde{c_\pm} = \nabla\left(D\nabla\widetilde{c_\pm} + \frac{zeD}{k_BT}\left(\mathrm{c}_\pm^0\nabla\tilde{\psi} + \widetilde{c_\pm}\nabla\psi^0\right) - \boldsymbol{v}\widetilde{c_\pm}\right), \tag{10}$$

$$\nabla(\varepsilon\nabla\tilde{\psi}) = (\mathrm{ez}_-\widetilde{c_-} + ez_+\widetilde{c_+}). \tag{11}$$

Since the application of the external electric field results in the transport of ions to the surface, the perturbed surface charge density ($\widetilde{\Sigma_s}$) is not constant, and is obtained by the model of Schurr (1964) (see also Leroy et al., 2008; Bücker et al., 2019):

$$i\omega\widetilde{\Sigma_\mathrm{s}} = \nabla\cdot(D_S\nabla\widetilde{\Sigma_\mathrm{s}} + \mu_\mathrm{s}\Sigma_\mathrm{s}^0\nabla\widetilde{\psi_s} - \boldsymbol{v}\widetilde{\Sigma_\mathrm{s}}). \tag{12}$$

where D_s is the diffusion coefficient at the Stern layer, and μ_s is the ion mobility, given by Einstein's relation ($\mu_s = D_s ez/k_BT$). The ∇ operators in Eq. 12 refer to tangential derivatives.

The equations for the perturbed part (Eq. 10, Eq. 11, and Eq. 12) were solved with the following boundary conditions: at the particle surface, the normal perturbed ionic flux is zero

($\boldsymbol{n}\cdot\widetilde{\boldsymbol{J_T}}\big|_{\text{surf}}=0$), and the perturbed potential is given by: $\boldsymbol{n}\left[-\varepsilon\nabla\tilde{\psi}+\varepsilon_{solid}\nabla\tilde{\psi}_{solid}\right]_{\text{surf}}=\widetilde{\Sigma_s}$, where ε_{solid} is the electric permittivity of the particle. Far from the particle, at $x=\pm 2.5L$, the perturbed concertation of both ions is zero, and $\tilde{\psi}\big|_{x=\pm 2.5L}=\mp\mathbf{2.5}|\boldsymbol{E_0}|L$. At $y=L$, we used insulating boundary conditions for both $\widetilde{\boldsymbol{J_T}}$ and $\tilde{\psi}$. The full set of boundary conditions for the equilibrium and perturbed parts are presented in Fig. 1, and the list of model parameters is provided in Table 1.

The equations for the solid domain were not affected by the advection flux. The equilibrium electrical potential ψ^0_{solid} is constant through the solid and equal to the potential at the grain's surface. The perturbation potential is determined by the Poisson equation $\nabla\cdot\left(\varepsilon_{solid}\nabla\tilde{\psi}_{solid}\right)=0$, and continuity between the surface and solid potential is ensured ($\tilde{\psi}_{solid}=\tilde{\psi}|_{\text{surface}}$).

Table 1: Model parameters[1]

Parameter	Description	Unit	Value
a	Grain radius	μm	5.0
$c^0_{\pm}$	Bulk concentration	mol m^{-3}	1.0
D	Diffusion coefficient at the bulk solution	m^2 s^{-1}	1.26×10^{-9}
D_s	Diffusion coefficient at the Stern layer	m^2 s^{-1}	1.26×10^{-10}
E_0	Magnitude of applied field	V m^{-1}	50.0
L	Domain length	μm	50.0
Σ^0_d	Net surface charge density	C m^{-2}	0.002
Σ^0_s	Surface charge density at the Stern layer	C m^{-2}	0.008
ε	Electric permittivity of the electrolyte	F m^{-1}	$80\varepsilon_0$
ε_{solid}	Electric permittivity of the solid	F m^{-1}	$4\varepsilon_0$
ε_0	Vacuum permittivity	F m^{-1}	8.85×10^{-12}

[1]All the model parameters, except the domain length, were taken from Bücker et al. (2019).

The model's implementation was performed using COMSOL Multiphysics, a finite element code for the solution of coupled partial differential equations (COMSOL, 2018). Considering that the polarization occurs near the particle surface, and strongly decays with distance, and following Bücker et al. (2019), the following mesh was constructed: around the

particle, we used a boundary-layer mesh, consisting of rectangular elements with a size of $\pi r_0/400 \approx 39$ nm in the tangential direction. In the radial direction, the thickness of the mesh elements increases with a stretching factor of 1.17, from 4.8 nm at the surface, until the 8th element. The rest of the mesh is filled with triangular elements, ranging in size from 39 nm to 2500 nm ($\sim L/20$). We checked the stability by refining the mesh near the particle, where the solution is rapidly changing.

3 Results and Discussion

3.1 Effect of flow rate on the measured SIP signature of soil

The average ($n = 3$) electrical spectra for the six fluid fluxes tested in the experiments and their standard deviations are presented for the Quartz sand and the Hamra soil in Fig. 2 and Fig. 3, respectively. For both porous materials, the maximum difference between the mean σ' of the six flow rates is small ($\sim 3\%$), and within the range of the standard deviation (Fig. 2a and Fig. 3a). These results indicate that the impact of fluid flow (at the tested flow rate range) on the σ' is small. As the flow rate increases, a consistent decrease in the low-frequency ($<$ 1 Hz) σ'' and in the relaxation time is observed (Fig. 2b and Fig. 3b). The maximum decrease between the quadrature conductivity at the peak frequency (σ''_{peak}) is $\sim 17\%$ and ~20% for the Quartz sand and the Hamra soil, respectively. At frequencies higher than the peak frequency (larger than 1 Hz), σ'' is similar for the different flow rates. To test if the impact of water flow on the SIP response of the porous media is reversible two scenarios were considered. In the first, flow rate was increased and SIP signal was recorded at different velocities. In the second, flow rate was decreased and SIP measurements were taken at the same velocities as before. The results show that similar flow rates yield similar electrical spectra, regardless of the direction of change in the flow rate, i.e., the impact of flow on electrical spectra is reversible (see the markers and dash lines in Fig. 2 and in Fig. 3).

In Fig. 2d and in Fig. 3d, we present the measured σ'' around the first relaxation frequency (0.01 to 10 Hz), together with the fitted Cole-Cole model (Eq. 3). Overall, there is a good agreement between the measured spectra and the Cole-Cole model, with a root mean square error (RMSE) that ranges from 0.026 μS/cm to 0.031 μS/cm for the Quartz, and from 0.038 μS/cm to 0.063 μS/cm for the Hamra soil.

The relative change in chargeability (m) and in the Cole-Cole time constant (τ) are presented as a function of the water flux in Fig. 4a and Fig. 4b, respectively. The Cole-Cole

exponent (c, see Eq. 3) ranged between 0.55 and 0.62, and between 0.58 and 0.63 for the Quartz sand and the Hamra soil, respectively, with no correlation to the water flux. The chargeability (related to the magnitude of polarization) decreases with water flux (Fig. 4a), and the maximum difference between the chargeability at zero flux and at the highest flux is $\sim 30\%$ for both the Quartz sand and Hamra soil. The time constant (τ) also decreases with the water flux. The relative change in τ is similar between the Quartz sand and the Hamra soil, with a maximum decrease of $\sim 55\%$ (Fig. 4b).

3.2 Results from numerical simulations

The quadrature conductivity as a function of frequency is shown for different flow rates in Fig. 5a. We do not show the in-phase conductivity, as it is practically constant (changes smaller than 0.5%) for all flow rates (similar results were obtained in the experiments, see Fig. 2a and Fig. 3a). The results demonstrate that as the flow rate increases, the quadrature conductivity decreases, and the critical frequency (the frequency of the peak polarization) increases. Fig. 5b shows a falling sigmoidal trend between the relative quadrature conductivity at the peak frequency and the Péclet number (Pe), where $\mathrm{Pe} = v_\infty a/D$ and v_∞ is the fluid velocity far from the particle. A similar falling sigmoidal trend is observed between τ and Pe (Fig. 5c). In Fig. 5d, we show the quadrature conductivity for the case of no-slip boundary condition ($\sigma''_{\mathrm{no-slip}}$). Note that we plot $\sigma''_{\mathrm{no-slip}}$ for all velocities as in the case of slip boundary conditions (Fig. 5a). Except for a very small decrease in $\sigma''_{\mathrm{no-slip}}$ with water velocity at frequencies higher than 1kHz, the impact of fluid flow on the $\sigma''_{\mathrm{no-slip}}$ is negligible.

To explain the decrease in τ with fluid velocity, we calculate the EDL length at different fluid velocities. To calculate the EDL radius, we followed the Debye- Hückel approach (Stumm & Morgan, 1996), where the Debye screening length defines the EDL length (κ^{-1}) at which the potential drop is $\frac{\psi^0_{\mathrm{surface}}}{\psi^0(\kappa^{-1})} = e \approx 2.72$, where $\psi^0_{\mathrm{surface}}$ is the equilibrium surface potential, and $\psi^0(\kappa^{-1})$ is the equilibrium potential at the Debye length. To accurately find the location where the potential is $\psi^0_{\mathrm{surface}}/e$, a very fine mesh is needed, especially since the change in the potential drop due to fluid flow is relatively small, and because for the case of zero fluid flow, $\kappa^{-1} \approx 10nm$. Therefore, for all velocities, we calculate the potential drop between the same two nodes in the mesh, the first at the particle surface and the second at a distance of $10nm$ from the surface. In other words, regardless of the fluid velocity, the potential drop is defined by

$$\zeta = \frac{\psi^0_{\text{surface}}}{\psi^0(r = a + 10nm)}. \quad (13)$$

As in the Debye- Hückel model for the EDL, we consider an exponential relationship between the potential and the EDL length and calculate the relative EDL radius using

$$r_{EDL} = \frac{\ln(\zeta_{v=0})}{\ln(\zeta)}. \quad (14)$$

While for the case of zero velocity, the EDL length is symmetric with respect to the particle (i.e., the EDL radius is the same, regardless of the angle θ (see Fig. 6b)), for non-zero velocities, the EDL deformed, and the radius is a function of θ. In Fig. 6a, we show the average change in the EDL length $\left(\delta L = \frac{L - L_{v=0}}{L_{v=0}}\right)$ where

$$L = \frac{1}{\pi} \int_{-\pi/2}^{\pi/2} r_{EDL}(\theta) d\theta. \quad (15)$$

In Fig. 6a, we show that as the velocity increases, the average EDL radius (δL) decreases. At low Pe numbers (Pe < 0.3), the decrease in δL is small, and at higher Pe, the reduction is linear on a semi-log plot (i.e., exponential decay). Since τ is governed (among other parameters) by the size of the EDL, the decrease in δL, explains the decline in τ with velocity (see Fig. 5c).

Fig. 6b demonstrates the EDL around the modeled spherical particle at three different velocities. Note that here, the EDL is the region between the particle surface and r_{EDL} (see Eq. 14) (to allow visualization, we amplify the EDL thickness in the radial direction). At zero velocity, r_{EDL} is symmetrically distributed around the particle. As the velocity increases, r_{EDL} is decreasing in the northern hemisphere and increases in the southern hemisphere. The average surface potential of the particle ($|\langle\psi^0_{\text{surface}}\rangle| = \frac{1}{\pi}\int_{-\pi/2}^{\pi/2}\left|\psi^0_{\text{surface}}\right|d\theta$) is also affected by the advection flux and as can be seen in Fig. 6c, $|\langle\psi^0_{\text{surface}}\rangle|$ decreases with velocity. Since the quadrature conductivity and the surface potential are related (Kremer et al., 2016), the reduction in $|\langle\psi^0_{\text{surface}}\rangle|$ with water velocity, can explain the observed decrease in quadrature conductivity.

3.3 Comparison between experimental data and numerical simulations

Qualitatively, there is an agreement between the experimental data and the numerical simulations regarding the impact of fluid flow on the SIP signature of porous media. In both cases, the polarization magnitude and the time constant decrease with fluid velocity, and the impact on the in-phase conductivity is negligible (Fig. 4 and Fig. 5). In Fig. 5b, we compare the experimental and simulated quadrature conductivity at the peak frequency (σ''_{peak}) for different Pe numbers. The results show that the numerical simulations overestimate the impact of water flow on the σ''_{peak} with a maximum decrease of $\sim 20\%$ and $\sim 80\%$ in σ''_{peak} for the experimental and numerical data, respectively. In addition, the numerical simulation overestimates the impact of water flow on τ with a maximum decrease of $\sim 60\%$ and $\sim 85\%$ in τ for the experimental and numerical data, respectively (Fig. 6c).

We suggest that the numerical simulations overestimate the impact of water flow on the polarization magnitude and time constant because the imposed slip boundary conditions for the Stokes equations (see section 2.2) overestimate the advection flux at the particle surface. The slip boundary condition means that water molecule near the particle surface is not subject to adhesion forces, and as a result, the velocity of water at the surface, e.g., at an angle parallel to the mean velocity vector (in our case at $\theta = 0$, see Fig. 6b) is identical to v_∞. For the case of no-slip boundary conditions, the maximum velocity (i.e., at $\theta = 0$) as a function of distance from the particle surface is given by the classical Stokes solution to the Navier-Stokes equations (Pnueli & Gutfinger, 1992):

$$\frac{v}{v_\infty} = 1 - \frac{3a}{4r} - \frac{a^3}{4r^3}. \tag{16}$$

At the EDL edge (in our case 10 nm), the ratio v/v_∞ is ~ 0.0018. Since the SIP method is sensitive to the polarization of the EDL, such low velocities, and as a result, low advection flux in the EDL are not expected to influence the SIP signature. Indeed, for the no-slip boundary condition, the quadrature conductivity was not affected by the advection flux (see Fig. 5d).

Based on the above, we speculate that in natural porous media, such as those tested here, the velocity at the particle surface should be described by partial slip boundary conditions where the water velocity at the surface is between zero and v_∞. Studies on water flow at the

nanometer scale show that the slippage of water on surfaces depends on the wettability of the surface and its roughness (Granic and Zhu ,2002; Cottin-Bizonne et al., 2003; Barrat and Bocquet, 2007). In particular, Vanson et al. (2017) showed that surface roughness introduces slippage at the solid-fluid interface in porous media, which would otherwise have a no-slip boundary condition. We expect that the relationship between advection flux and the SIP signature of porous media will depend on the surface roughness and wettability of the solid phase. This is the focus of our future research.

3.4 Limitations

This study elucidates the impact of pore water velocity on the spectral induced polarization signature of porous media. The experimental data demonstrates that as the velocity increases, polarization and time constant decrease. The numerical model is in qualitative agreement with the experimental data, but it overestimates it. Several model assumptions should be highlighted. First, as discussed above, the slip boundary conditions for water flow overestimate the water velocity at the particle surface and should be further investigated. The appropriate slip length (an extrapolated distance inside the solid at which the tangential velocity define as zero) should be determined according to the porous media surface roughness and wetness. Second, due to numerical instability, we didn't couple Stokes' equations with the electric field (i.e., we neglect electroosmotic flow). Under realistic conditions, applying an external electric field to the EDL drives electroosmotic flow that results in an advection flux in the EDL (even when the bulk velocity is zero), affecting the SIP signature of the porous media. Nonetheless, the fact that we consider slip boundary conditions allows advection flux to develop in the EDL, and while the magnitude of the flux might not be precise, its structure and impact on the SIP signature are properly captured.

4 Conclusions

The low-frequency polarization and the Cole-Cole time constant of porous media decrease as the bulk fluid velocity increases. A flow-through experiment and a mechanistic model for SIP have been implemented to reveal the role of ion advection flux in the low-frequency electrical properties of the porous media. Based on the results, we suggest that the observed decrease in polarization is attributed to the effect of ion advection flux on the EDL's electrical structure. The demonstrated sensitivity of the SIP signature to ion advection flux in the EDL opens an exciting new direction in noninvasive studies of the fluid field at the solid-

liquid interfaces of charged surfaces. This topic recently gained vast interest in various fields, such as flow in porous media, microfluidics, electrochemistry, fuel cells, and more. In addition, the results highlight the need to consider fluid velocity in the interpretation of the SIP signature of porous media.

5 Acknowledgments

The data are available in Zenodo at http://doi.org/10.5281/zenodo.4785240. This research was partially funded by the Israeli Ministry of Sciences and Technology (Grant number 3-15500). We thank the editor X. Sanchez-Vila and the associate editor L. Slater for their effort and constructive comments. We also would like to thank M. Bücker and two anonymous reviewers for their effort and detailed review, which significantly improve this paper.

References

Adamson, A. W., & Gast, A. P. (1997). *Physical chemistry of surfaces* (6th ed.). New York: Wiley.

Bazant, M. Z. (2011). Induced-Charge Electrokinetic Phenomena. In *Electrokinetics and Electrohydrodynamics in Microsystems* (pp. 221–297). Vienna: Springer Vienna. https://doi.org/10.1007/978-3-7091-0900-7_7

Bocquet, L., & Barrat, J.-L. (2007). Flow boundary conditions from nano- to micro-scales. *Soft Matter*, *3*(6), 685–693. https://doi.org/10.1039/B616490K

Bücker, M., & Hördt, A. (2013). Analytical modelling of membrane polarization with explicit parametrization of pore radii and the electrical double layer. *Geophysical Journal International*, *194*(2), 804–813. https://doi.org/10.1093/gji/ggt136

Bücker, M., Flores Orozco, A., Undorf, S., & Kemna, A. (2019). On the Role of Stern- and Diffuse-Layer Polarization Mechanisms in Porous Media. *Journal of Geophysical Research: Solid Earth*, *124*(6), 5656–5677. https://doi.org/10.1029/2019JB017679

COMSOL. (2018). COMSOL Multiphysics. Computer software, COMSOL AB, Sweden.

Coperey, A., Revil, A., Abdulsamad, F., Stutz, B., Duvillard, P. A., & Ravanel, L. (2019). Low-Frequency Induced Polarization of Porous Media Undergoing Freezing: Preliminary Observations and Modeling. *Journal of Geophysical Research: Solid Earth*, *124*(5), 4523–4544. https://doi.org/https://doi.org/10.1029/2018JB017015

Cottin-Bizonne, C., Barrat, J. L., Bocquet, L., & Charlaix, E. (2003). Low-friction flows of liquid at nanopatterned interfaces. *Nature Materials*, *2*(4), 237–240. https://doi.org/10.1038/nmat857

DeLacey, E. H. B., & White, L. R. (1981). Dielectric response and conductivity of dilute suspensions of colloidal particles. *J. Chem. Soc., Faraday Trans. 2*, *77*(11), 2007–2039. https://doi.org/10.1039/F29817702007

Dukhin, S. S., & Shilov, V. N. (1974). *Dielectric phenomena and the double layer in disperse systems and polyelectrolytes*. New York: Wiley.

Joseph, P., Cottin-Bizonne, C., Benoît, J. M., Ybert, C., Journet, C., Tabeling, P., & Bocquet, L. (2006). Slippage of water past superhydrophobic carbon nanotube forests in microchannels. *Physical Review Letters*, *97*(15), 156104. https://doi.org/10.1103/PhysRevLett.97.156104

Jougnot, D., Leroy, P., & Cosenza, P. (2010). Spectral Induced Polarization of partially saturated clay-rocks: a mechanistic approach. *Geophysical Journal International*, *180*, 210–224. https://doi.org/10.1111/j.1365-246X.2009.04426.x

Kemna, A., Binley, A., Cassiani, G., Niederleithinger, E., Revil, A., Slater, L., et al. (2012). An overview of the spectral induced polarization method for near-surface applications. *Near Surface Geophysics*, *10*(6), 453–468. https://doi.org/10.3997/1873-0604.2012027

Kessouri, P. and Furman, A. and Huisman, J. and Martin, Tina and Mellage, Adrian and Ntarlagiannis, Dimitrios and Bücker, Matthias and Ehosioke, Solomon and Fernandez, Perrine and Flores Orozco, Adrián and Kemna, Andreas and Nguyen, F. and Pilawski, T. an, E. (2019). Induced polarization applied to biogeophysics: recent advances and future prospects. *Near Surface Geophysics*, *17*(10), 595–621. https://doi.org/10.1002/nsg.12072

Kimak, C., Ntarlagiannis, D., Slater, L. D., Atekwana, E. A., Beaver, C. L., Rossbach, S., et al.

(2019). Geophysical Monitoring of Hydrocarbon Biodegradation in Highly Conductive Environments. *Journal of Geophysical Research: Biogeosciences*, *124*(2), 353–366. https://doi.org/https://doi.org/10.1029/2018JG004561

Kremer, T., Schmutz, M., Leroy, P., Agrinier, P., & Maineult, A. (2016). Modelling the spectral induced polarization response of water-saturated sands in the intermediate frequency range (102-105 Hz) using mechanistic and empirical approaches. *Geophysical Journal International*, *207*(2), 1303–1312. https://doi.org/10.1093/gji/ggw334

Lauga, E., Brenner, M., & Stone, H. (2007). Microfluidics: The no-slip boundary condition. In *Springer Handbooks* (pp. 1219–1240). Springer. https://doi.org/10.1007/978-3-540-30299-5_19

Leroy, P., Revil, A., Kemna, A., Cosenza, P., & Ghorban, A. (2008). Complex conductivity of water-saturated packs of glass beads. *Journal of Colloid and Interface Science*, *321*(1), 103–117. https://doi.org/10.1016/j.jcis.2007.12.031

Leroy, P., Weigand, M., Mériguet, G., Zimmermann, E., Tournassat, C., Fagerlund, F., et al. (2017). Spectral induced polarization of Na-montmorillonite dispersions. *Journal of Colloid and Interface Science*, *505*, 1093–1110. https://doi.org/10.1016/j.jcis.2017.06.071

Lyklema, J. (Ed.). (1995). Electrokinetics and Related Phenomena. In *Solid-Liquid Interfaces* (Vol. 2, pp. 4–135). Academic Press. https://doi.org/https://doi.org/10.1016/S1874-5679(06)80007-3

Mellage, A., Smeaton, C. M., Furman, A., Atekwana, E., Rezanezhad, F., & Van Cappellen, P. (2018). Linking spectral induced polarization (SIP) and subsurface microbial processes: Results from sand column incubation experiments. *Environmental Science & Technology*, *52*(4), 2081–2090. https://doi.org/10.1021/acs.est.7b04420

Newman, J. S., & Thomas-Alyea, K. E. (2004). *Electrochemical systems* (3rd ed.). John Wiley & Sons. https://doi.org/10.1017/CBO9781107415324.004

Pnueli, D., & Gutfinger, C. (1992). *Fluid Mechanics*. Cambridge University Press. https://doi.org/10.1017/CBO9781139172561

Revil, A. (2013). Effective conductivity and permittivity of unsaturated porous materials in the frequency range 1 mHz-1GHz. *Water Resources Research*, *49*(1), 306–327. https://doi.org/10.1029/2012WR012700

Revil, A., & Florsch, N. (2010). Determination of permeability from spectral induced polarization in granular media. *Geophysical Journal International*, *181*(3), 1480–1498. https://doi.org/https://doi.org/10.1111/j.1365-246X.2010.04573.x

Revil, A., Atekwana, E., Zhang, C., Jardani, A., & Smith, S. (2012). A new model for the spectral induced polarization signature of bacterial growth in porous media. *Water Resources Research*, *48*(9). https://doi.org/https://doi.org/10.1029/2012WR011965

Ristenpart, W. D., Aksay, I. A., & Saville, D. A. (2007). Electrohydrodynamic flow around a colloidal particle near an electrode with an oscillating potential. *Journal of Fluid Mechanics*, *575*, 83–109. https://doi.org/10.1017/S0022112006004368

Schurr, J. M. (1964). On the Theory of the Dielectric Dispersion of Spherical Colloidal Particles in Electrolyte Solution1. *The Journal of Physical Chemistry*, *68*(9), 2407–2413. https://doi.org/10.1021/j100791a004

Schwartz, N., Levy, L., Carmeli, B., & Radian, A. (2020). Spectral induced polarization of

clay-oxide hybrid particles. *Journal of Colloid and Interface Science*, *577*, 173—180. https://doi.org/10.1016/j.jcis.2020.05.029

Shilov, V. N., Delgado, A. V, Gonzalez-Caballero, F., & Grosse, C. (2001). Thin double layer theory of the wide-frequency range dielectric dispersion of suspensions of non-conducting spherical particles including surface conductivity of the stagnant layer. *Colloids and Surfaces A: Physicochemical and Engineering Aspects*, *192*(1), 253–265. https://doi.org/https://doi.org/10.1016/S0927-7757(01)00729-4

Slater, L., Ntarlagiannis, D., Personna, Y., & Hubbard, S. (2007). Pore-scale spectral induced polarization signatures associated with FeS biomineral transformations. *Geophysical Research Letters*, *34*(21). https://doi.org/10.1029/2007gl031840

Soldi, M., Jougnot, D., & Guarracino, L. (2018). An analytical effective excess charge density model to predict the streaming potential generated by unsaturated flow. *Geophysical Journal International*, *216*(1), 380–394. https://doi.org/10.1093/gji/ggy391

Stumm, W., & Morgan, J. J. (1996). *Aquatic Chemistry : Chemical Equilibria and Rates in Natural Water* (3rd ed.). New York: Chichester: Wiley.

Tarasov, A., & Titov, K. (2013). On the use of the Cole-Cole equations in spectral induced: Polarization. *Geophysical Journal International*, *195*(1), 352–356. https://doi.org/10.1093/gji/ggt251

Titov, K., Komarov, V., Tarasov, V., & Levitski, A. (2002). Theoretical and experimental study of time domain-induced polarization in water-saturated sands. *Journal of Applied Geophysics*, *50*(4), 417–433. https://doi.org/10.1016/S0926-9851(02)00168-4

Titov, K., Kemna, A., Tarasov, A., & Vereecken, H. (2004). Induced polarization of unsaturated sands determined through time domain measurements. *Vadose Zone Journal*, *3*(11), 1160–1168. https://doi.org/10.2136/vzj2004.1160

Tsukanov, K., & Schwartz, N. (2020). Relationship between wheat root properties and its electrical signature using the spectral induced polarization method. *Vadose Zone Journal*, *19*(1). https://doi.org/10.1002/vzj2.20014

Vanson, J.-M., Boutin, A., Klotz, M., & Coudert, F.-X. (2017). Transport and adsorption under liquid flow: the role of pore geometry. *Soft Matter*, *13*(4), 875–885. https://doi.org/10.1039/C6SM02414A

Vaudelet, P., Schmutz, M., Franceschi, M., & Bégassat, P. (2011). Changes in induced polarization associated with the sorption of sodium, lead, and zinc on silica sands. *Journal of Colloid and Interface Science*, *360*, 739–752. https://doi.org/10.1016/j.jcis.2011.04.077

Vinegar, H. J., & Waxman, M. H. (1984). Induced polarization of shaly sands. *Geophysics*, *49*(8), 1267–1287. https://doi.org/10.1190/1.1441755

Virtanen, P., Gommers, R., Oliphant, T., Haberland, M., Reddy, T., Cournapeau, D., et al. (2020). SciPy 1.0: fundamental algorithms for scientific computing in Python. *Nature Methods*, *17*(2), 1–12. https://doi.org/10.1038/s41592-019-0686-2

Volkmann, J., & Klitzsch, N. (2010). Frequency-Dependent Electric Properties of Microscale Rock Models for Frequencies from One Millihertz to Ten Kilohertz. *Vadose Zone Journal*, *9*(11), 858–870. https://doi.org/10.2136/vzj2009.0162

Weigand, M., & Kemna, A. (2019). Imaging and functional characterization of crop root systems using spectroscopic electrical impedance measurements. *Plant and Soil*, *435*,

201–224. https://doi.org/10.1007/s11104-018-3867-3

Weller, A., Breede, K., Slater, L., & Nordsiek, S. (2011). Effect of changing water salinity on complex conductivity spectra of sandstones. *Geophysics*, *76*(5), F315–F327. https://doi.org/10.1190/geo2011-0072.1

Willmott, G. (2008). Dynamics of a sphere with inhomogeneous slip boundary conditions in Stokes flow. *Physical Review E*, *77*(5), 055302. https://doi.org/10.1103/PhysRevE.77.055302

Zhang, C., Slater, L., Redden, G., Fujita, Y., Johnson, T., & Fox, D. (2012). Spectral Induced Polarization Signatures of Hydroxide Adsorption and Mineral Precipitation in Porous Media. *Environmental Science & Technology*, *46*(8), 4357–4364. https://doi.org/10.1021/es204404e

Zhang, L., & Wang, M. (2017). Electro-osmosis in inhomogeneously charged microporous media by pore-scale modeling. *Journal of Colloid and Interface Science*, *486*, 219–231. https://doi.org/https://doi.org/10.1016/j.jcis.2016.09.057

Zhu, Y., & Granick, S. (2002). Limits of the Hydrodynamic No-Slip Boundary Condition. *Physical Review Letters*, *88*(10), 106102. https://doi.org/10.1103/PhysRevLett.88.106102

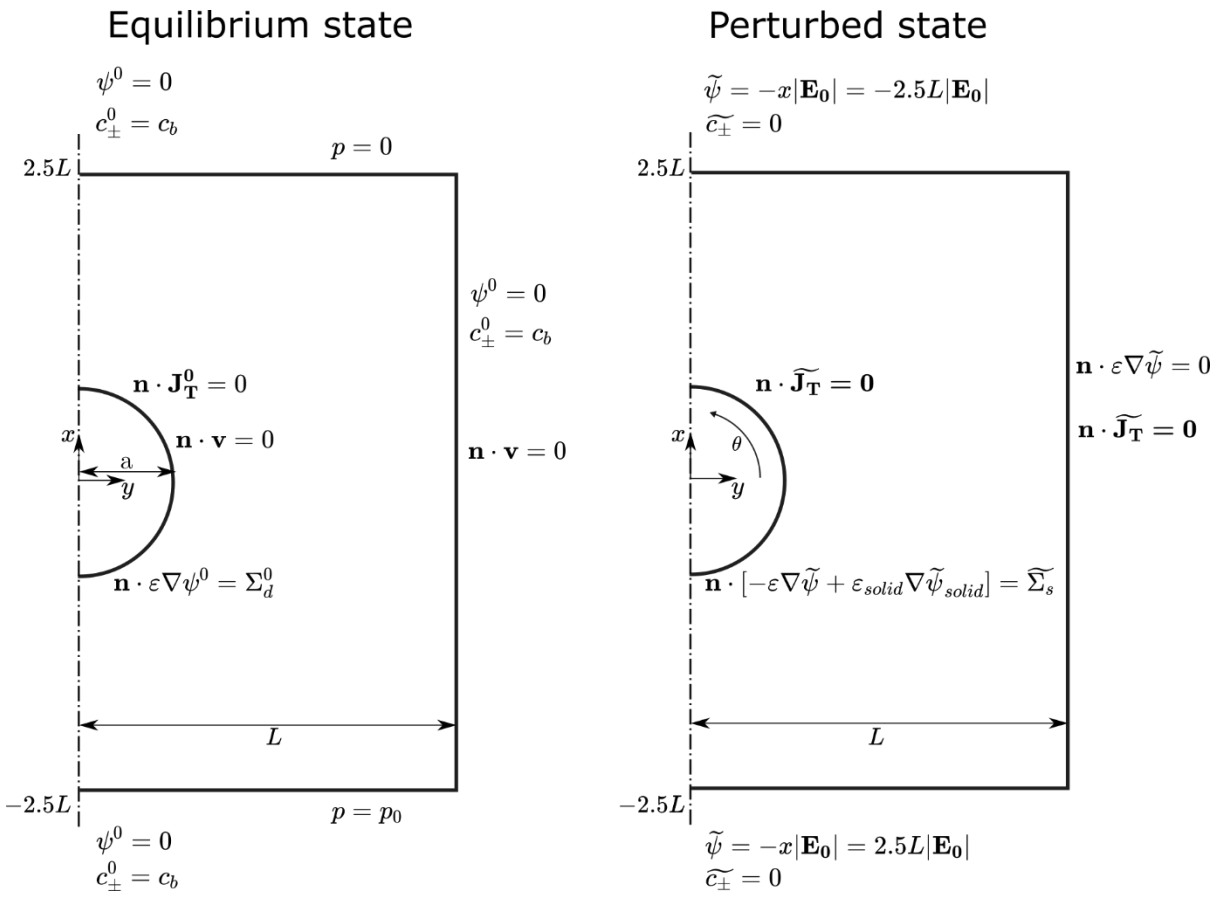

Figure 1: Model domain and boundary conditions for the equilibrium (left) and perturbed (right) states. The model is 2-dimensional axisymmetric, so the half-circle is translated to a 3-dimensional sphere.

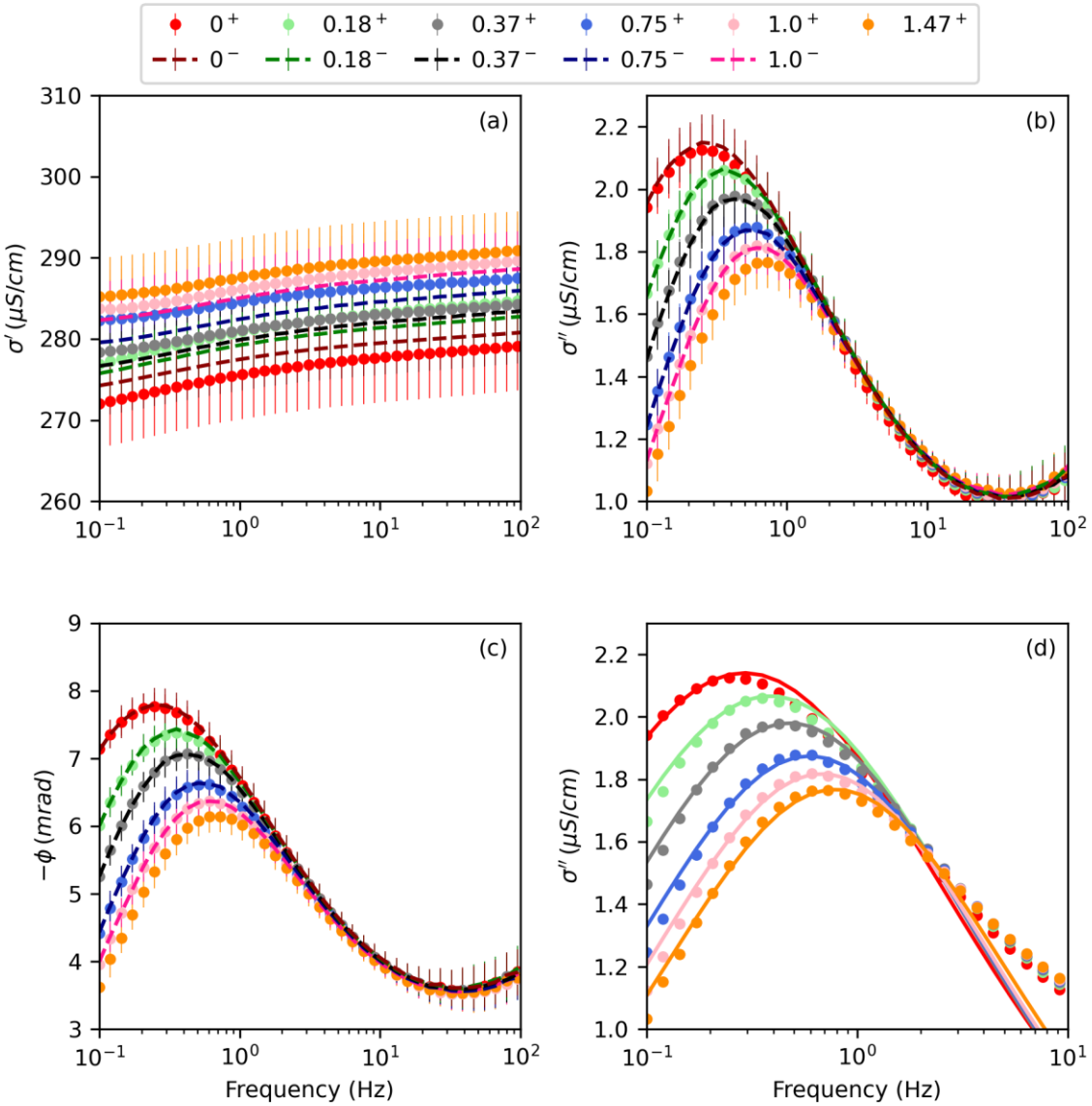

554

Figure 2: The electrical conductivity as a function of frequency (Hz) for the Quartz sand, presented for six different velocities (the velocities given in the legend are in cm/min). In panels (a) to (c), the markers represent results obtained while increasing the velocity, and the dashed lines represent results obtained while decreasing the velocity (this is also represented by the plus and minus superscript in the legend). (a) The effect of fluid velocity on the in-phase conductivity, σ'. Notably, no effect is observed. (b) The quadrature conductivity, σ'' as a function of frequency. A decrease with fluid velocity in σ'' and time constant is observed (note the shift to the right in the spectra, with increasing velocity). (c) The phase shift as a function of fluid velocity. (d) Comparison between the quadrature conductivity experimental data (symbols) and the Cole-Cole model results (solid lines).

555

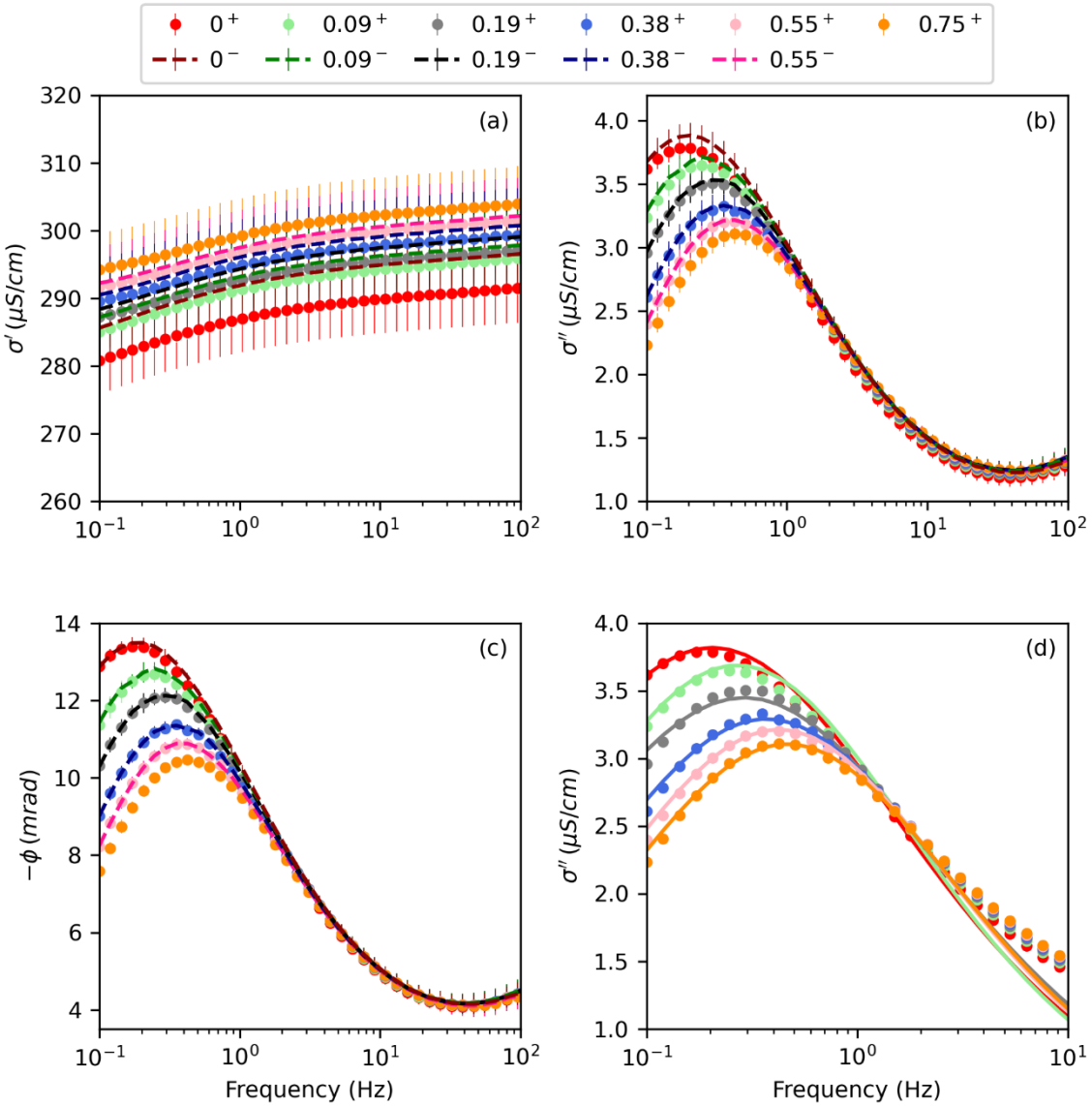

556

Figure 3: The electrical conductivity as a function of frequency (Hz) for the Hamra soil, presented for six different velocities (the velocities given in the legend are in cm/min). In panels (a) to (c), the markers represent results obtained while increasing the velocity, and the dashed lines represent results obtained while decreasing the velocity (this is also represented by the plus and minus superscript in the legend). (a) The effect of fluid velocity on the in-phase conductivity, σ'. Notably, no effect is observed. (b) The quadrature conductivity, σ'' as a function of frequency. A decrease with fluid velocity in σ'' and time constant is observed (note the shift to the right in the spectra, with increasing velocity). (c) The phase shift as a function of fluid velocity. (d) Comparison between the quadrature conductivity experimental data (symbols) and the Cole-Cole model results (solid lines).

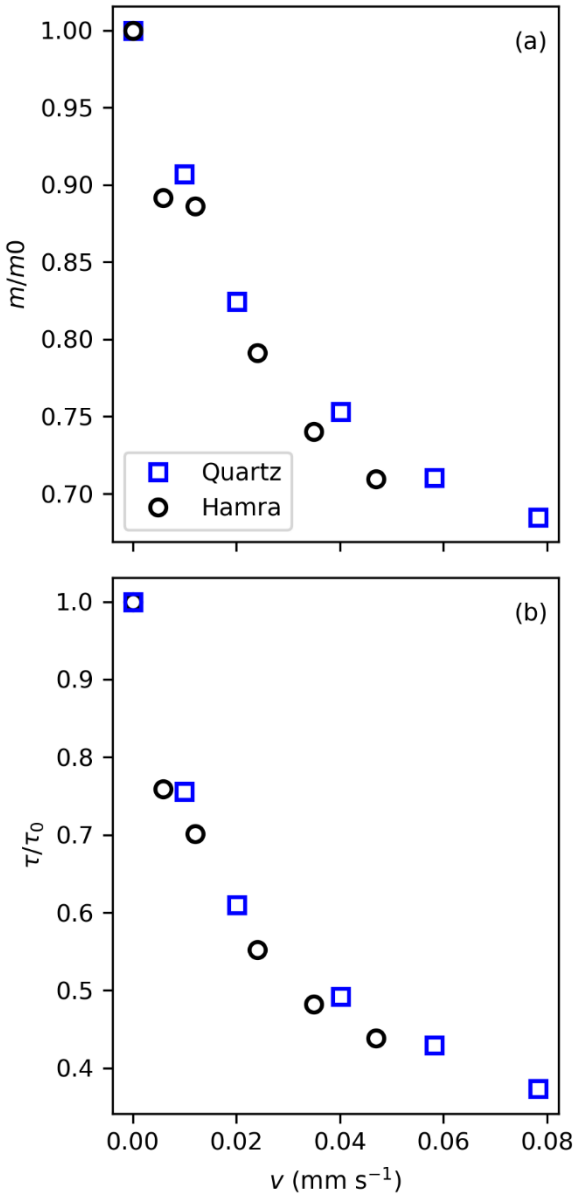

Figure 4: Cole-Cole model parameters as a function of the water flux for the Quartz sand and Hamra soil. (a) the relative change in chargeability (m; a measure of polarization), and (b) the relative change in the time constant (τ), as a function of the water flux.

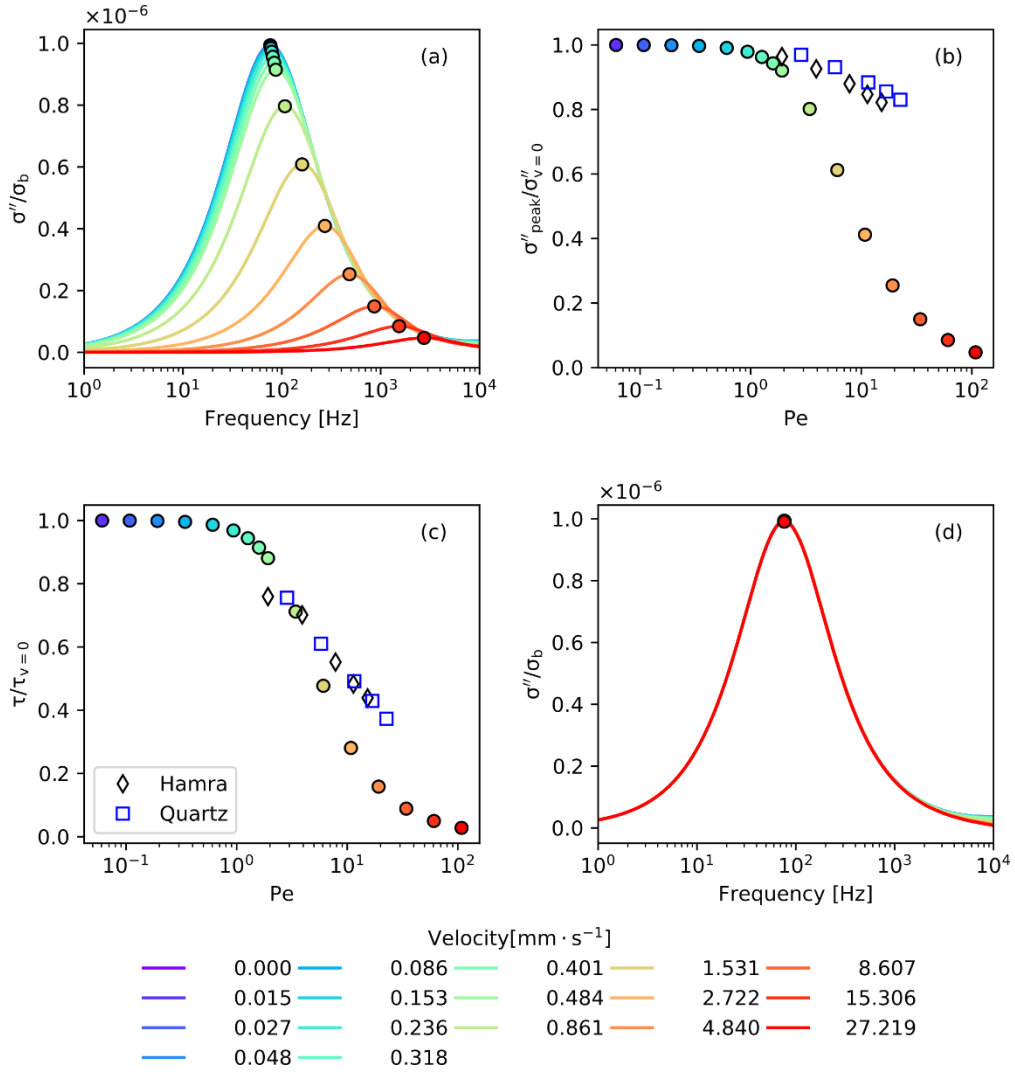

560

561

562

Figure 5: Quadrature conductance divided by the bulk conductance (relative conductance). (a) The relative conductance as a function of frequency, presented for different velocities. (b) The relative conductance at the peak frequency as a function of velocity, and (c) the time constant as a function of velocity. The dots in panels (b) and (c) represent the data from the numerical simulation, and the solid line represent the resultsfrom the numerical simulations. Note that to calculate the Pe number for the experimental data, we used the mean particle size which is $160\ \mu m$ and $120\ \mu m$, for the Quartz sand and the Hamra soil, respectively. We used the same diffusion coefficient as in the numerical simulation (see Table 1).

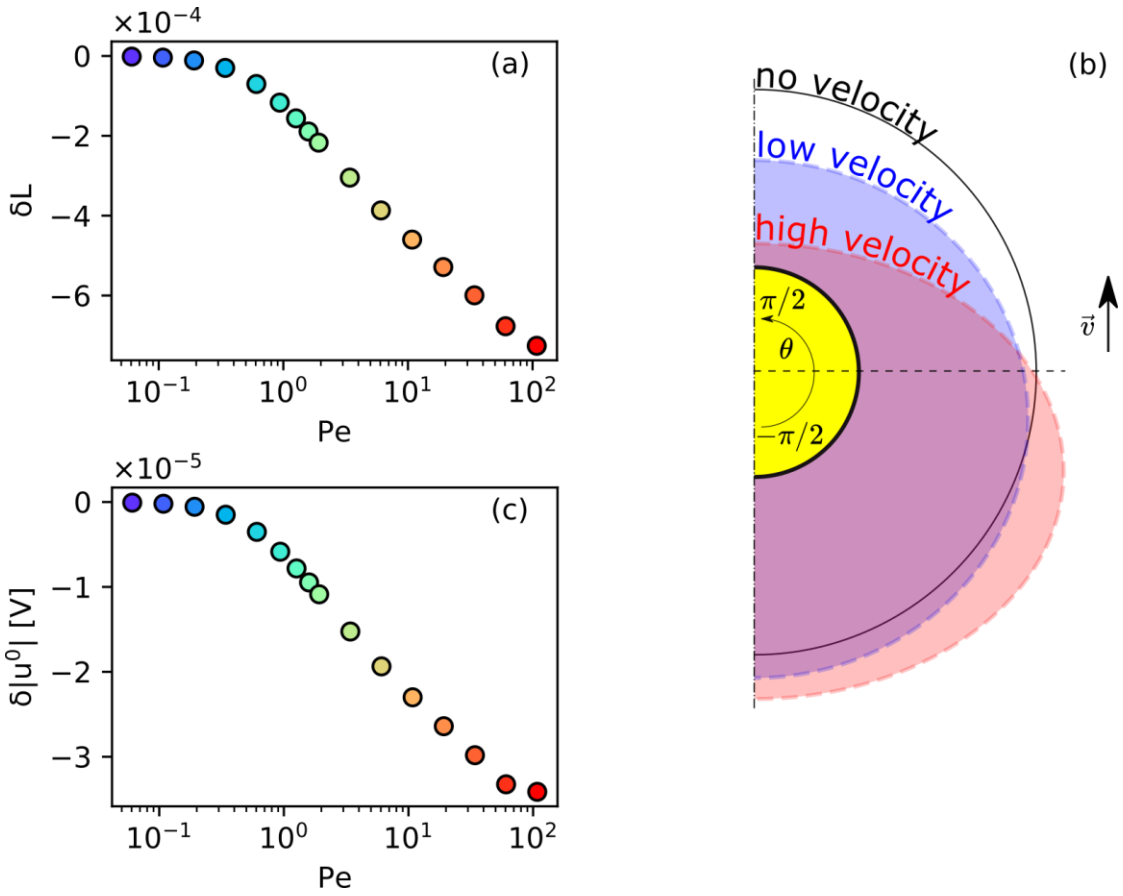

Figure 6: (a) Relative change in the EDL length as a function of the Pe number. (b) The EDL's radius (r_{EDL}, see Eq. 14) at three velocities. The radius of the EDL is exaggerated in the radial direction to allow visualization (at zero velocity, the particle radius is 500 times larger than r_{EDL}). (c) Change in the average surface potential of the particle as a function of the Pe number.